Peer-reviewed version available at *ISPRS Int. J. Geo-Inf.* **2017**, *6*, 4; doi:10.3390/ijgi6010004

Article

Crustal and Upper Mantle Density Structure Beneath the Qinghai-Tibet Plateau and Its Surrounding Areas Derived from EGM2008 Geoid Anomalies

Honglei Li 1,2,* and Jian Fang 1

1 State Key Laboratory of Geodesy and Earth's Dynamics, Institute of Geodesy and Geophysics, Chinese Academy of Sciences, Wuhan 430077, China; jfang@whigg.ac.cn
2 University of Chinese Academy of Sciences, No. 19A Yuquan Road, Beijing 100049, China
* Correspondence: hlli@whigg.ac.cn; Tel.: +86-15072331377

Abstract: As the most active plateau on the Earth, the Qinghai-Tibet Plateau has a complex crust-mantle structure. Knowledge of the distribution of such a structure provides information for understanding the underlying geodynamic processes. We obtains a three-dimensional density model of crustal and upper mantle beneath Qinghai-Tibet plateau and its surrounding areas from the residual geoid anomalies using the Earth Gravitational Model (EGM) 2008. We estimate a refined density model by iterations, using an initial density contrast model. We confirm that the EGM2008 mission products can be used to constrain the crust-mantle density structures. Our major findings are: (1). At 300-400 km depth, high-D anomalies terminate around Jinsha River Suture (JRS) in the central TP, suggesting that the Indian plate has been reached over the Bangong Nujiang Suture (BNS) and almost reach to the JRS. (2). On the eastern TP, low-D anomalies at the depth of 0-300 km together with high-D anomalies at 400-670 km further verified the current eastward subduction of Indian plate. The ongoing subduction provides forces to the occurrences of frequent earthquakes and volcano. (3). At 600 km depth, low-D anomalies inside the TP illustrate the existence of hot weak material beneath there, contributing to the external material inward-thrusting.

Keywords: Qinghai-Tibet Plateau; geoid anomaly inversion; crustal and upper mantle density construction

---

1. Introduction

The Qinghai-Tibet Plateau is the highest and largest plateau in the world. Its average height is ~4500 meters and its area is ~2500000 km^2. As a response to the subduction of the lithospheric mantle of the Indian plate, large-scale crustal motion occurs in this area. It has complex crust-mantle structure[1]. Its crust thickness, on averages, is 65-70 km [2].Structure of crust and upper mantle in Tibet has obvious zoning characteristics, inhomogeneous distribution of the lower velocity in the crust and higher velocity in upper mantle[3]. Different models for the formation of the TP have been developed. Knowledge of crust and upper mantle structures beneath the TP is particularly informative for understanding the underlying formation. Some geophysical constraints regarding the velocity structure[4-7], the electrical structure[8, 9] and the thermal structure[10, 11] in this region have been obtained. However, few result of density structure of the whole plateau has been reported. Considering the fact that the Earth's density is the direct product of geodynamic, detailed density structure can give strong geophysical evidence for understanding the underlying geodynamic processes.

Peer-reviewed version available at ISPRS Int. J. Geo-Inf. 2017, 6, 4; doi:10.3390/ijgi6010004

Next to gravity, geoid is another sensitive physical quantity to the Earth interior density. Both of them play important roles in studying the Earth's interior density structures. The gravity of one point is inversely proportional to the square of the distance between that point and the source of the structure. As the depth increases, the amplitudes of gravity decrease rapidly and the gravity anomaly primarily reflects the shallow short-wavelength density changes. While another amount – geoid has a larger difference from the gravity. It is inversely proportional to the distance measuring from the source. It reflects the long-wavelength field characteristics of the density changes in the deep earth. Therefore, the geoid anomaly is often used to study the deep mantle density anomalies[12].

The absence of underground gravity observations in this region inhibits the density research progresses. However, with the development of various observation methods[13, 14], the high sensitivity, high resolution and global coverage gravity satellite measurements provide an effective means for the study of the Earth's interior density structure. The official Earth Gravitational Model EGM2008[15] has been publicly released by U.S. National Geospatial Intelligence Agency (NGA). This gravitational model is complete spherical harmonic degree and order 2159, and contains additional coefficients extending to degree 2190 and order 2159. It has an accuracy of 20 cm in mainland and 12 cm in Central-East China, 9 cm in Northern China and 24 cm in Western China at sea level[16]. In our work, we choose to use the geoid anomaly derived from the Earth Gravitational Model EGM2008 to perform the density inversion.

The study region of our interest is 75°E -115°E, 20°N -45°N. A method of gravitational modeling based on a spherical prism was proposed. In this work, objective function will be given based on the Lagrange multiplier method and the Tikhonov regularization theory[12]. Damped Least Square method is used during the inversion. Seismic velocities are to be imposed as a constraint. Finally, a three-dimensional density model of crustal and upper mantle beneath Qinghai-Tibet plateau and its surrounding areas is determined by the inversion of a set of geoid anomaly. This paper is closed with geodynamics analysis.

2. Methodology

2.1. Fundamental Equations

According to the famous Bruns formula[17], which describes the relationship between geoid height and the perturbing potential, for any point outside the Earth, the induced geoid height should be described in equation $N(P)=\dfrac{T(P)}{\gamma(P)}$, where $P(r,\varphi,\lambda)$ is the computation point; r, φ and λ are the radius, latitude, and longitude, respectively; $\gamma(P)$ is the normal gravity on the geodetic reference ellipsoid. The perturbing potential $T(P)$ is given by numerically integration composed by a set of spherical prisms, the so-called tesseroids, which bounded by two meridians, two parallels, and two concentric circles. So the approximate expression of geoid height developed by Heck and Size[18] based on tesseroids is described in equation (1).

$$N(P)=\frac{G\rho\Delta r\Delta\varphi\Delta\lambda}{\gamma(P)}\left[K_{000}+\frac{1}{24}\left(K_{200}\Delta r^2+K_{020}\Delta\varphi^2+K_{002}\Delta\lambda^2\right)+O\left(\Delta^4\right)\right] \tag{1}$$

Where G is Newton's constant of gravitation; ρ is the density contrast which is assumed constant within each tesseroid; $\Delta r=r_1-r_2$, $\Delta\varphi=\varphi_1-\varphi_2$, and $\Delta\lambda=\lambda_1-\lambda_2$ are the tesseroid dimensions in the radial and horizontal directions; K_{000}, K_{002}, K_{020}, K_{200} are the coefficients that depend on the relative positions of computation point and the geometrical center of the tesseroids which can be obtained in the article , $O\left(\Delta^4\right)$ is the landau symbol which indicates terms of the order 4 in Δr , $\Delta\varphi$, $\Delta\lambda$ that are omitted.

As the derivative of equations (1) is linear with respect to the density contrast ρ , thus a set of n calculated geoid anomalies caused by a model compose of m tesseroids can be written as:

$$N_{\rho(n\times1)}=G_{\rho(n\times m)}\rho_{(m\times1)} \tag{2}$$

Where ρ is the vector of estimated density contrast; N_ρ is the vector of geoid anomaly; G_ρ is the matrix of the sensitive function between density contrast and geoid anomaly

2.2. Density inversion

Aiming to get the density contrast derived from the gravitational observations, we established the objective function in Equation (4) based on the Lagrange multipliers theory, the method which has been used in Yellowstone Province geoid anomalies inversion[12]. This theory considers both the misfit error of the observation and the ridge regression error of the parameter. We need to minimize the objective function as follows:

$$L(\rho,\alpha)=\left(\rho-\rho_{apr}\right)^T W_\rho{}^T W_\rho\left(\rho-\rho_{apr}\right)+2\alpha^T W_d\left(G_\rho\rho-N_\rho\right) \tag{3}$$

Where ρ_{apr} is an initial model; W_ρ is the parameter-weighting matrix, as the geoid anomaly is inversely proportional to the distance of the source, in order to ensure that each tesseroids has the same probability on the matrix G_ρ, we use the matrix $W_\rho = diag\left(\frac{1}{(z+\varepsilon)^\beta}\right)$ to give the weight on the matrix G_ρ ,where z is the depth of each tesseroid, ε is a small constant to avoid singularity, β is a number that changes the weight of W_ρ ; W_d is the data weight matrix; α is Lagrange multipliers vectors. To minimize the objective function, we derived equation (3) with respect to ρ and α, with setting them equal to zeroes and we can obtain the solution as follows:

$$\begin{cases}\hat{\rho}=\rho_{apr}+\left(W_\rho{}^T W_\rho\right)^{-1} G_\rho{}^T W_d{}^T\left(W_d G_\rho\left(W_\rho{}^T W_\rho\right)^{-1} G_\rho{}^T W_d{}^T\right)^{-1} W_d\left(N^\rho-G_\rho\rho_{apr}\right)\\ \alpha=-\left(W_d G_\rho\left(W_\rho{}^T W_\rho\right)^{-1} G_\rho{}^T W_d{}^T\right)^{-1} W_d\left(N^\rho-G_\rho\rho_{apr}\right)\end{cases} \tag{4}$$

Where $\hat{\rho}$ is the estimated density contrasts. In order to solve the ill-posed inversion because of small singular values contained in the sensitivity matrix G_ρ, we add the constant μ to equation (4)

$$\hat{\rho}=\rho_{apr}+\left(W_\rho{}^T W_\rho\right)^{-1} G^T W_d{}^T\left(W_d G\left(W_\rho{}^T W_\rho\right)^{-1} G^T W_d{}^T+\mu I\right)^{-1} W_d\left(N_\rho-G\rho_{apr}\right) \tag{5}$$

Where μ is the regularization parameter, which can be determined by the Tikhonov regularization theory[19].

To obtain the best solution of equation (5), we consider solving it iteratively:

$$\hat{\rho}_{k+1}=\hat{\rho}_k+\Delta\hat{\rho}_k \tag{6}$$

where $\hat{\rho}_k$ is the density contrasts after the k^{th} iteration; For $k=0,1,2\cdots n$, where $\hat{\rho}_0$ is ρ_{apr} which is an induced initial density model given by a 3-D Vs model ; $\Delta\hat{\rho}_k$ is given as follows:

$$\Delta\hat{\rho}_k=\left(W_\rho{}^T W_\rho\right)^{-1} G^T W_d{}^T\left(W_d G\left(W_\rho{}^T W_\rho\right)^{-1} G^T W_d{}^T+\mu I\right)^{-1} W_d\left(N_\rho-G\hat{\rho}_k\right) \tag{7}$$

Peer-reviewed version available at *ISPRS Int. J. Geo-Inf.* **2017**, *6*, 4; doi:10.3390/ijgi6010004

Then, the process is searching for a solution that fits the observed data best. As an acceptance criterion, we use the root-mean-square (RMS) error of fitting errors function $E_1 = N_\rho - G_\rho \hat{\rho}_k$ is smaller than or equal to a constant value ε_1 . Another criterion for convergence is that $E_2 = \Delta\hat{\rho}_k / \hat{\rho}_k$ is smaller than a certain previously determined empirical value ε_2. The inversion may also be terminated after a pre-specified number of iterations.

3. Synthetic Tests

We carried out some synthetic models for our above proposal. Geoid forwarded from the designed density model. We simulated two synthetic models. M1 is a synthetic model of negative geoid anomaly caused by a low density material distribute from 150 km to 200 km in depth (Δr =50 km), with horizontal dimensions of ~1554 km and ~2109 km ($\Delta\varphi$=14° ,$\Delta\lambda$ =19°) and density contrast of -50 kg/m^3. M2 is a synthetic model of countered geoid anomaly caused by a low density on the right side and a high density on the left distribute from 600 km to 150 km in depth (Δr =450 km), with horizontal dimensions of 333 km ($\Delta\varphi$=$\Delta\lambda$ =3°) and density contrast of -50 kg/m^3.We added 5% Gaussian random noises to the synthetic data that will be referred to as the "observed geoid data". We implemented two tests that consider two different kinds of models, whose inversion parameters are β =0.9; ε_1 =10^{-4}; ε_2 = 10^{-2}. The final iterations, modeling errors and fitting errors are listed in Table 1.

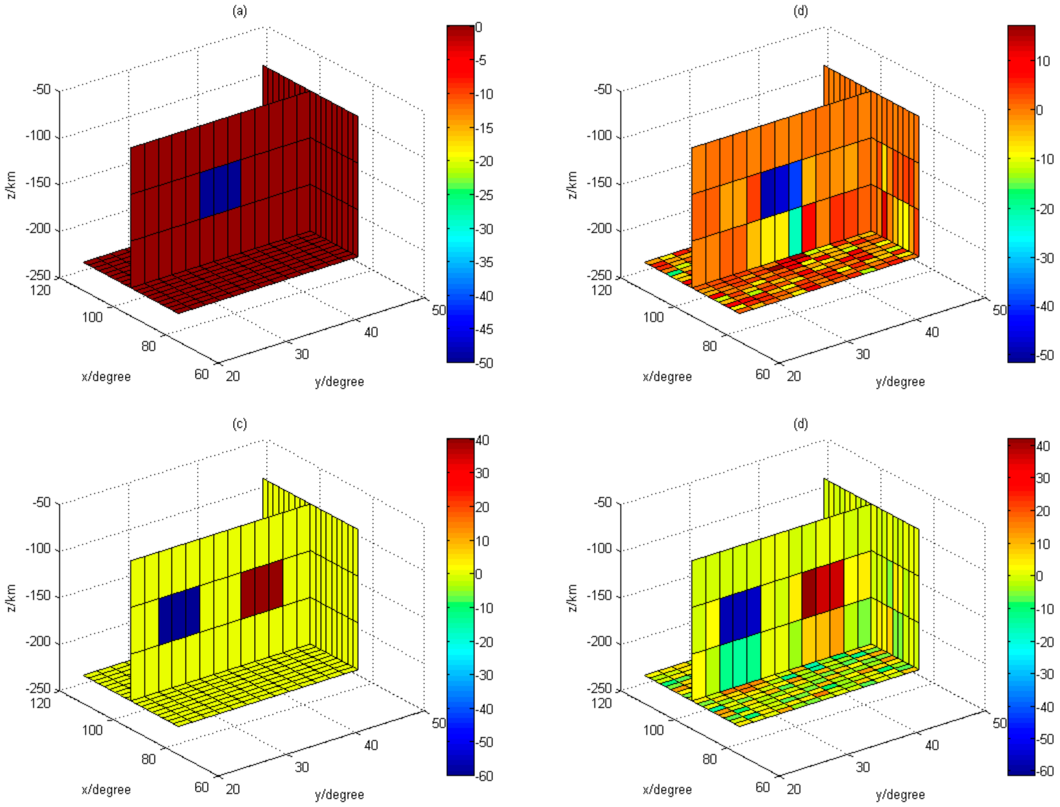

Figure 1. (a): Synthetic model 1; (b): Estimated model 1; (c): Synthetic model 2; (d): Estimated model 2

In these two cases, we can always get the acceptable results regardless of the noise. The important parameters are shown in Table 1. The synthetic tests proved the validity and correctness of our inversion method.

doi:10.20944/preprints201610.0062.v1

Peer-reviewed version available at *ISPRS Int. J. Geo-Inf.* **2017**, *6*, 4; doi:10.3390/ijgi6010004

Table1. Conditions and results for three different synthetic inversion models

Observations($\overline{n}_\rho$)	**Iniatial($\hat{\rho}_0$)**	**L-corner(μ)**	**Iterations(k)**	**ME**	**FE**
G1+5%noise	0	225	7	2.79	0.0134
G2+5%noise	0	225	5	2.63	0.0132

Where G1 is the geoid (N_ρ^{1}) data for M1; similar to G2; ME is the modelling errors RMS ($\hat{\rho}_k$ -ρ_{ture}); FE is the fitting errors RMS($G_\rho\hat{\rho}_k - N_\rho$); ρ_{ture} is the true model; RMS is the root mean square

4. The Eastern Qinghai-Tibetan Plateau

4.1. Geological Outline

The study region is defined by coordinates 75°E and 115°E, 20°N and 50°N as shown in figure 2. Several studies regarding the structure of upper mantle in Qinghai-Tibet plateau have been carried out in the past few years: the crust thicknesses are ~70-75 km under south (S) Tibet, and 60-65 km under north (N), northeast (NE) and southeast (SE)Tibet. The Indian crust collides with Tarim Basin at 80°E and it has reached the BNS belt at 88°E (in the west if 90°E)[7]. Weak zones are in the upper crust of Himalaya, in the middle crust of southern Lhasa, in the middle and lower crust of Northern Lhasa, and in their middle and lower crust of Qiangtang and Songpan-Ganzi[20]. The northern TP can be characterized with a sharp Moho offset beneath the ATF, a steep plateau margin, and a major south-directed thrust fault. Likewise, the characteristics for southeastern TP are the Low-gradient topography change; the crustal LVZ extends over a long distance, and gradual Moho change at the plateau margin[20]. The crust/mantle interface beneath Tibet is anisotropic[1]. In our work, a detailed three-dimensional crustal and upper mantle density structure blow the Qinghai-Tibet plateau is our objective.

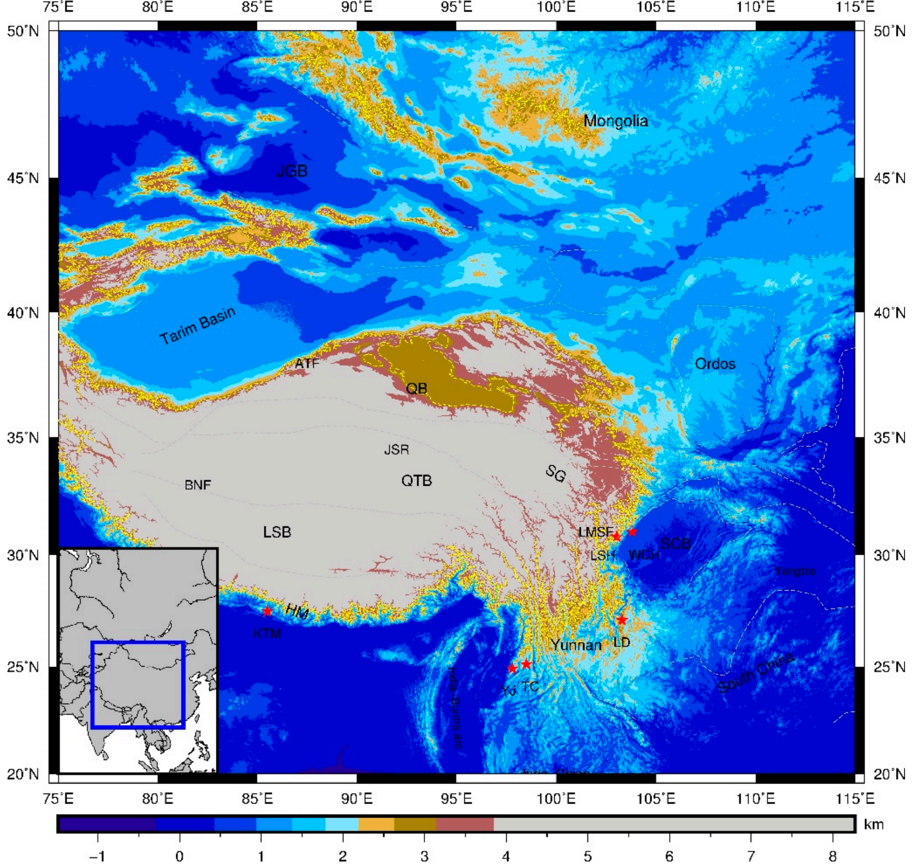

Figure 2. Topography and major tectonics of the density study area; in the figure: MBT- Main Boundary Thrust, MCT-Main Central Thrust, BNF-Bangong Nujiang Fault, JRS- Jinsha River Suture,

ATF- Altun Tagh Fault, LMSF- Longmen Shan HM-Himalaya Block,LSB-Lhasa Block; QTB-Qiangtang Block, QB-Qaidam Block, SG-Songpan Ganzi Block, Tarim Basin –Tarim Basin, Ordos- Ordos Block, SCB-Sichuan Basin; Red Stars are the locations of earthquakes that have happened in recent years and the volcano in the study area respectively: WCH-2008,8.0M,earthquake epicenter Wenchuan, LSH- 2013,7.0M,earthquake epicenter Lushan, LD-2014,6.5M,earthquake epicenter Ludian, YJ- 2011,5.8M,earthquake epicenter Yingjiang; TC-Tengchong Volcano[21].

4.2. Data Processing

The three-dimensional density model of the crust and uppermost mantle is determined by the inversion of geoid anomalies from the Earth Gravitational Model (EGM) 2008 expanded up to degree 180 using a starting density model derived from a seismic S-wave model.

We calculated the geoid height data at the sea level with the spherical harmonic expansion up to degree and order N = 180 from the global Earth model EGM2008 (figure 3a). The geoid model which has an accuracy of 0.15 m RMS worldwide is computed with respect to the WGS-84[15]. It provides a uniform and global field which enables the interpretation at both regional and global scales.

However, the anomaly is generated by all sources within the Earth. It represents the responses to all the interface undulations and in-homogenous density blow the Earth surface. With the aim of delineating the crustal and upper mantle density variation, the signal of topographic masses above the sea level, the effects of density interface (lithosphere interface, Moho interface, Sedimentary interface) variations, the influence of density changes below the upper mantle should be reduced before the inversion.

$$n_\rho = N_\rho - N_\rho^{\,1} - N_\rho^{\,2} - N_\rho^{\,3} - N_\rho^{\,4} - N_\rho^{\,5} \tag{8}$$

Where N_ρ is the vector of observed geoid anomaly; $N_p^{\,1}$ is the vector of density changes below the upper mantle geoid effect; $N_\rho^{\,2}$ is the vector of topographic geoid effect; $N_\rho^{\,3}$ is the vector of sedimentary interface variation geoid effect; $N_\rho^{\,4}$ is the vector of Moho interface variation effect; $N_\rho^{\,5}$ is the vector of lithosphere interface variation geoid effect; n_ρ is the vector of residual geoid anomalies caused by the upper mantle density variation.

The influence of density changes below the uppermost mantle (figure 3b) is given by Order and Degree 2-6 of EGM2008 based on the point mess source theory developed by Bowin[22] $z_n = R/n-1$, where z_n is the depth of the source; R is the radius of the Earth; n is the Order and Degree of the spherical harmonic coefficient . The topographic effects (figure3c) are estimated through the 1 arc min global relief model of the Earth's surface ETOPO1[23] (figure3C) with a set of spherical prism discretization based on Equation 2. The layer-specific density values are 2670 kg/m^3 and 1640 kg/m^3 for rocks above and below surface, respectively. The same strategy applied to the collected 0.5° *0.5° sedimentary undulations (figure3D), where the average sediment depth is 4 km and the density contrast between sediment and crust is 200 kg/cm^3[24].

We then obtain the 1° x1°Moho interface (figure3E) included in the global crustal model crust1.0 [25], and the 1° x1° Lithosphric interface coming from the global lithospheric model litho1.0 [26] (figure3F), respectively. The average depth for Moho is 35 km and the density contrast between crust and uppermost mantle is 420 kg/cm^3 and the average depth for lithosphere is 100 km and the density contrast between crust and uppermost mantle is 10 kg/cm^3 [24]. We use the same strategy as described above.

doi:10.20944/preprints201610.0062.v1

Peer-reviewed version available at *ISPRS Int. J. Geo-Inf.* **2017**, *6*, 4; doi:10.3390/ijgi6010004

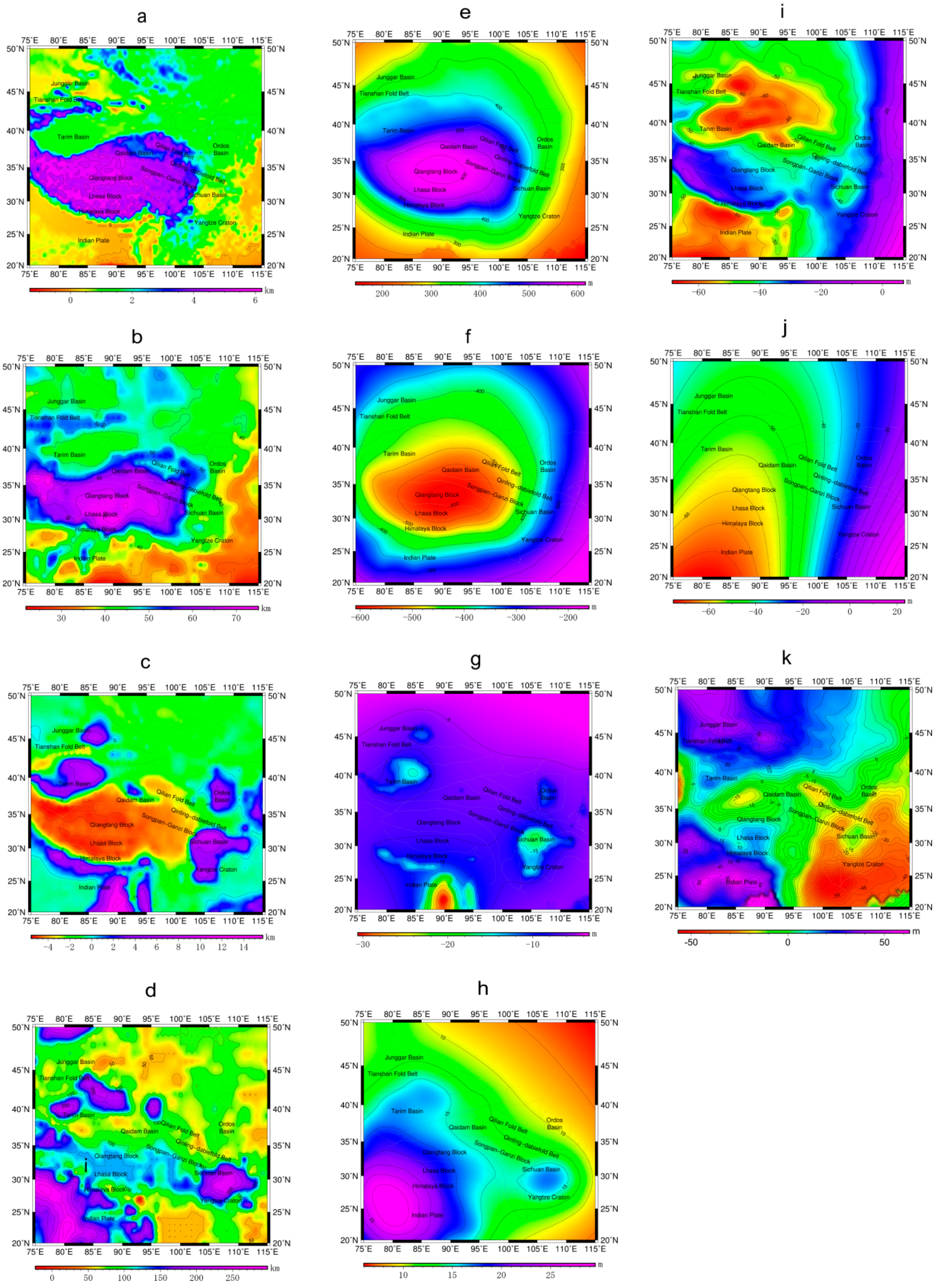

Figure 3. (a) Topography of the TP; (b) Moho depth of the TP; (c) Sediment depth of the TP; (d) Effect of Moho interface variation; (e) Effect of topographic masses; (f) Effect of Sedimentary interface variation; (g) Lithosphere depth of the TP; (h) Effect of lithospheric interface variation; (i) Geoid anomaly from EGM2008 up to degree 180; (j) Geoid anomalies from EGM2008 of degree 2-6; (k) The residual geoid anomaly after reducing the above motioned contributions.

The effects are illustrated in figure 3a-f. The contribution of topographic masses is the largest with amplitude of approximately 650 m. The effect amplitude of the basins is smaller (~570 m) with respect to those of the topographic effect. The largest amplitude of the lithospheric effect is in the southwest of the study area which is almost close to 30 m. The sedimentary effects in Sichuan basin, Qaidam basin and Indian arc basin are obvious. The amplitudes can be up to 25m.

The residual geoid anomaly is shown in figure 3g. It is computed after reducing the above motioned contributions, with value of ±55 m. As shown in figure 3f, the residual geoid has the trend of "positive-negative-positive" from the southwest to northeast.

4.3. Density Inversion and Results

The model of the crustal and upper mantel layers which was used to forward model the geoid is discretized by tesseroid blocks[18], having a uniform density in each tesseroid. The model is composed by six layers image the density structures of Qinghai-Tibet plateau up to 670 km depth, with of about ~222 km (2°) in horizontal and variable thickness and depths in vertical. It has the thickness of 100 km in the first five layers and 170 km in the last layer. The transition depths of the model are 50 km, 150 km, 250 km, 350 km, 450 km, and 600 km, respectively

The initial density model for the inversion is based on seismic velocities from the tomography using the velocity–density relation empirical formula form derived by Woodhouse and Dziewonski[27]

$$\delta\rho = \alpha\delta V_S^{\ 2} \tag{9}$$

Where $\delta\rho$ is the density contrast in unit of g/cm^3; δV_S is the velocity anomalies in unit of km/s based on the seismic Vsv model derived from seismic tomography developed by Simmons et al.[28]and a starting average Vs Model TNA-SNA; α is the transfer coefficient with the empirical value of 3.13×10^5.

We inverted the residual geoid anomaly based on equation (7). The initial density contrast $\hat{\rho}_0$ for the inversion is $\delta\rho$. We refined the density model by iterative inversion to reduce the fitting error. A stopping rule is set as $\varepsilon_1 = 0.1\ \mathrm{m}$ or the iteration number greater than 20. That is to say that only if the RMS of different between the calculated gradients and the observation no larger than 0.1m or the iterations no larger than 20, the corresponding density model can be considered reasonable. After 20 iterations, we obtain the final acceptable density model. As the illustrated in figure 4a, the fitting error decreased with the iterations and after about 20 iterations, the inversion is almost stable. The final geoid anomaly residual is shown in Figure 4b. Most of the final residuals are the high frequency errors.

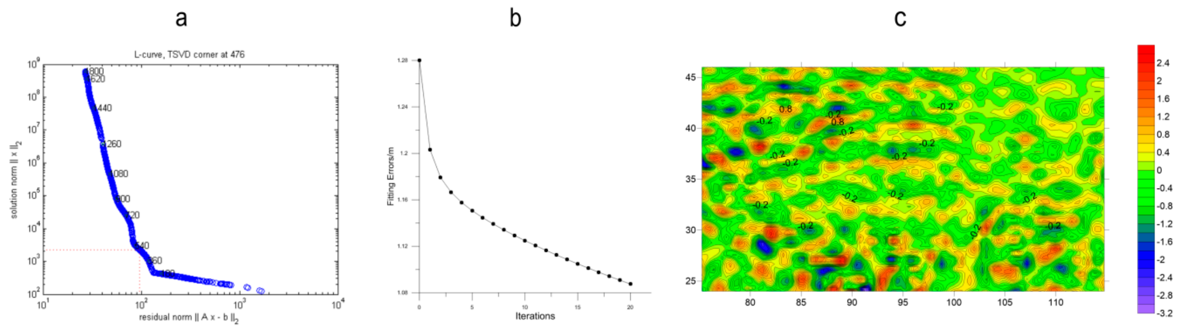

Figure 4. (a) L-curve (b) The fitting error decreased with the iterations; (c) The final geoid anomaly residual, unit (m)

Our results reveal some large-scale, structurally controlled density variations at depth as illustrate in figure 5(a)-(f).

Across the first layer, density anomalies that are at the average depth of 50 km, referring to the crust, vary intensely. As is shown in figure 5(a), in the eastern TP, lower density (low-D) anomalies in the crust terminate around the LMS. In the southern TP, low-D anomalies in the crust extend over a long distance. In the northern TP, crustal low-D anomalies stop beneath the ATF. These results agree well with the lower velocity zones (LVZs) found by previous studies[7, 29]. Low-D anomalies are also found in the Qilian fold belt. It is in line with the result by the high precision underground gravity anomalies[30]. Besides, low-D anomalies with the amplitude up to -20 $\mathrm{kg/m^3}$ block on the eastern TP from north to south. Meanwhile, high density (high-D) anomalies with the amplitude up to 60 $\mathrm{kg/m^3}$ are clustering on the western TP. From west to east in the study area, crustal high-D anomalies are in the Tianshan, Tarim basin, Qiadam basin, and the Sichuan basin. It could be the reason of hard basements there. High-D anomalies can also be found in the southwestern TP (Himalaya block, Lhasa block, Qiangtang block) extending downward to 300 km. From the analysis of recent earthquakes' (WCH- 2008,8.0M,earthquake epicenter Wenchuan, LSH-2013,7.0M,earthquake epicenter Lushan, LD-2014,6.5M,earthquake epicenter Ludian, YJ-2011,5.8M,earthquake epicenter Yingjiang;) locations in this region, all of them occurred in the transition zones between high-D and low-D density anomalies in the crust.

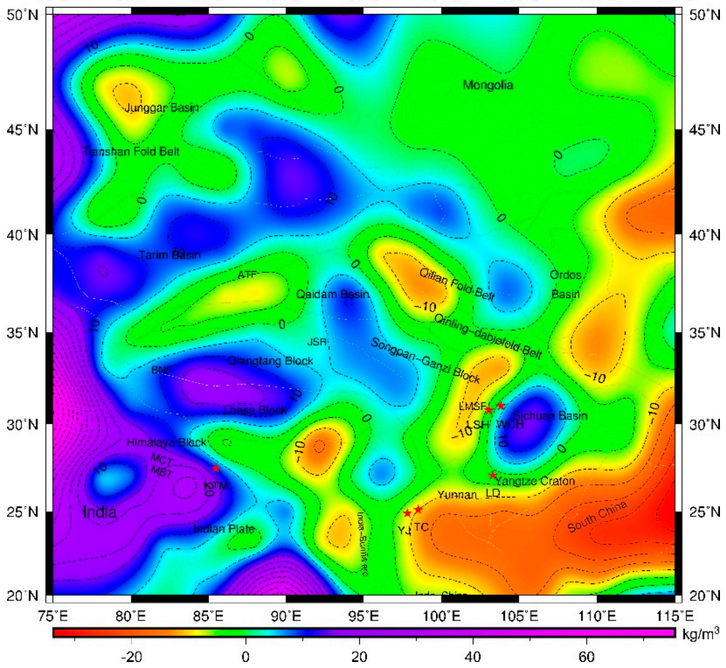

Figure5. (a) Map of horizontal density distribution at 50 km depth

Peer-reviewed version available at ISPRS Int. J. Geo-Inf. 2017, 6, 4; doi:10.3390/ijgi6010004

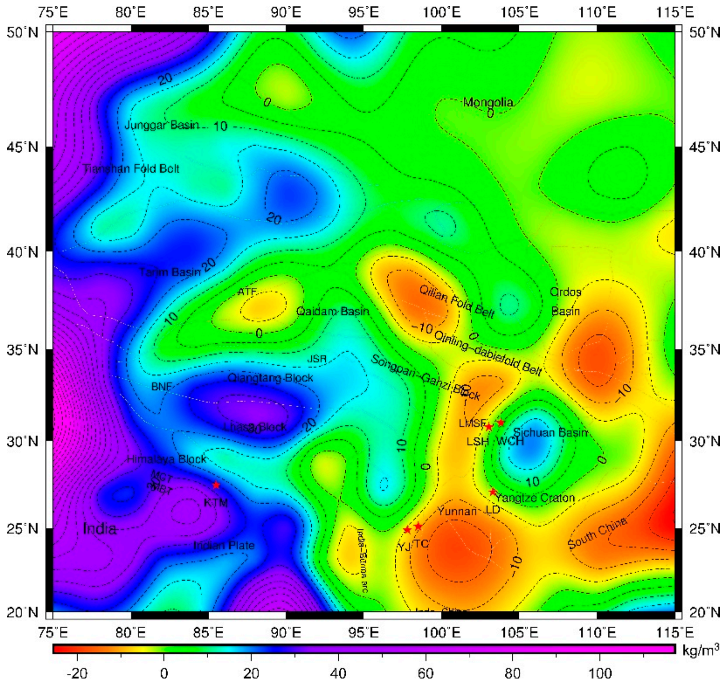

Figure5. (b) Map of horizontal density distribution at 150 km depth

In the second layer, the characteristics of density anomalies at average depth of 150 km, which belong to the upper mantle, (figure5b), agree well with the results of the first ones, except that the higher densities in the middle Songpan-Ganzi decrease in terms of amplitude. On southeastern Tibet, below Yunan province in particular, blocked Low-D anomalies form a closed loop. Furthermore, earthquakes were still in the transition zones between high-D and low-D anomalies in the uppermost mantle.

Density anomalies features in the third layer (figure5c), with average depth of 250 km, are analogous to the results shown in figure 5b, except that it refers to the amplitude of the anomalies. Prominent low-D anomalies site still near the periphery of the TP higher density. High-D anomalies below the southern Qiangtang and northern Lhasa always exist from 0 km to 300 km, with stretching to deeper than 300 km.

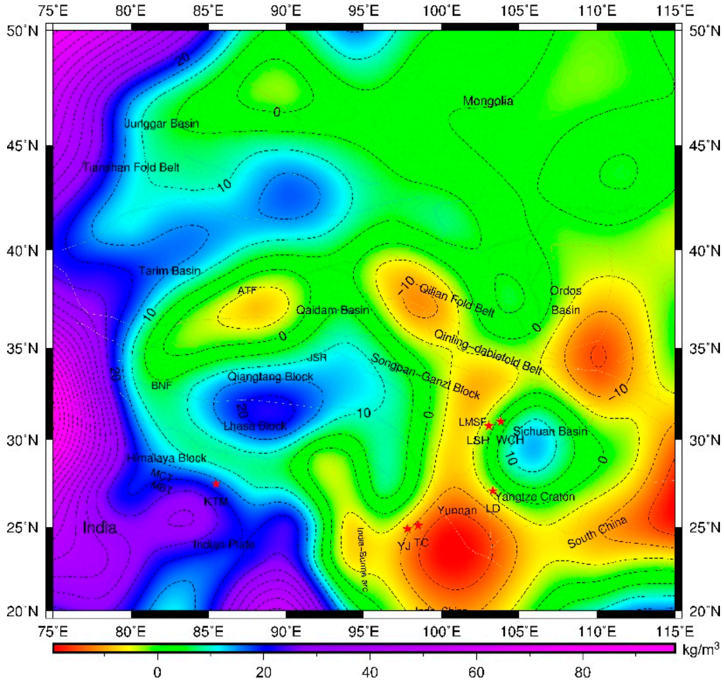

Figure5. (c) Map of horizontal density distribution at 250 km depth

Peer-reviewed version available at ISPRS Int. J. Geo-Inf. 2017, 6, 4; doi:10.3390/ijgi6010004

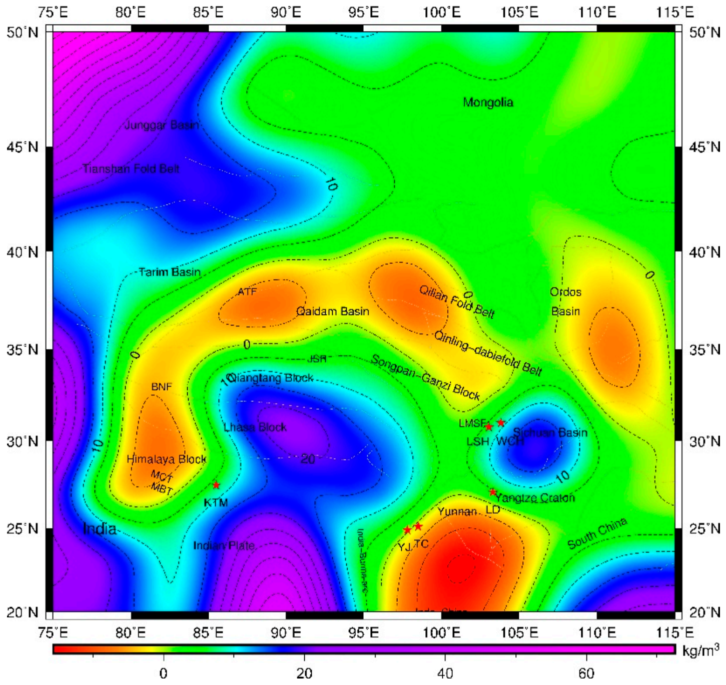

Figure5. (d) Map of horizontal density distribution at 350 km depth

In the fourth layer, density anomalies that are at average depth of 350 km, which belong to the 300-400 km mantle, change a lot They exhibit an apparently weak density zones pattern across the TP, with EW strike in central Tibet, rotating to approximately NW-SE direction towards eastern Tibet, which is similar to the low Pn velocity belt extend from west to east beneath Qiangtang and Songpan-Ganze, then turns southword beneath eastern TP and further south [31, 32]. Obvious high-D anomalies (~40 kg/m^3) present in the southern TP and on the northwestern TP. In the southern TP, the blocked high density anomalies have already reached over the BNS and almost reach to the JRS. On the northwestern TP, the high density anomaly should be the south-dipping subduction of the Asian lithospheric plate.

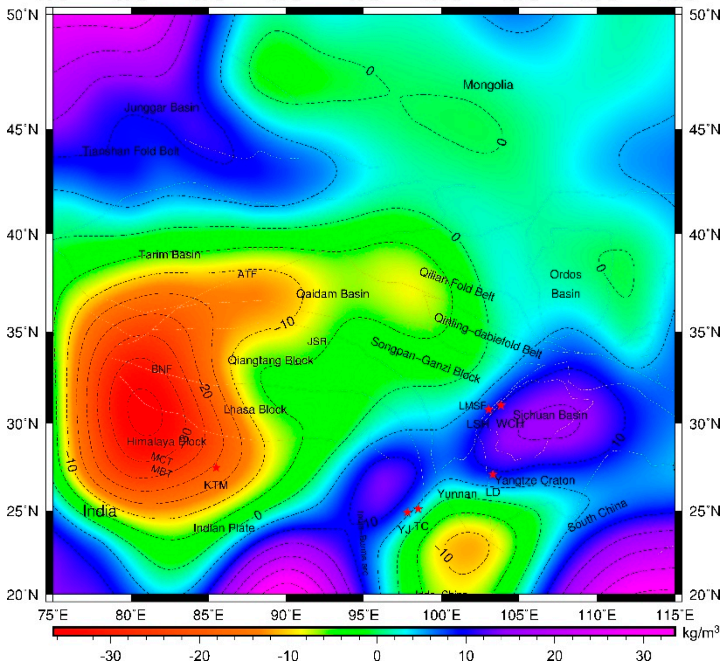

Figure5. (e) Map of horizontal density distribution at 450 km depth

Peer-reviewed version available at *ISPRS Int. J. Geo-Inf.* **2017**, *6*, 4; doi:10.3390/ijgi6010004

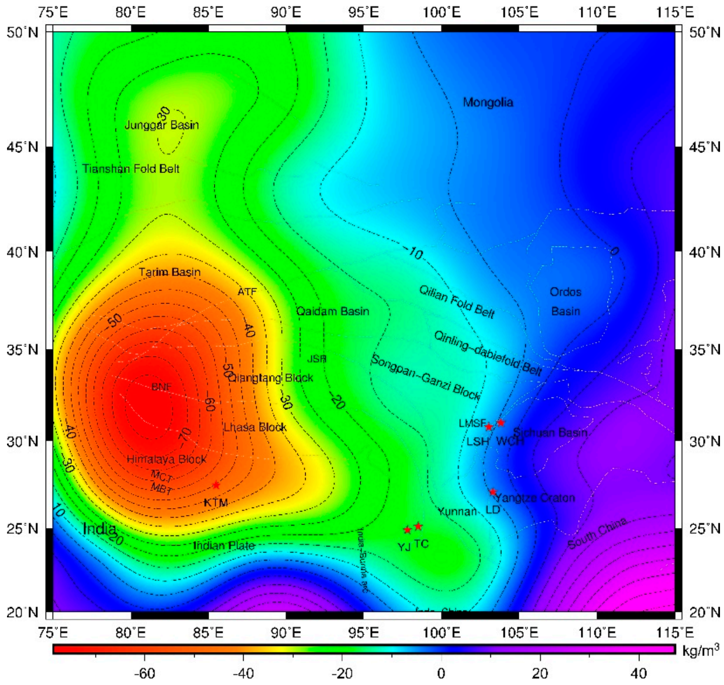

Figure5. (f) Map of horizontal density distribution at 600 km depth

In the fifth layer, density anomalies that are at average 450 km depth, which belong to the 400-500 km upper mantle, have a striking change. Low density anomalies are in the whole TP. On the southeastern TP, three high density anomaly zones (HDZs) with the amplitude up to 30 kg/m^3 obviously present in the mantle transition zone along the Bruma arc. On the eastern of those three HDZs, a weak HDZ with the value approximate -5 kg/m^3 emerged.

In the sixth layer, density anomalies that are at average 600 km depth, which belong to the 500-670 km mantle transition zone, are different from the anomalies discussed above. It presents the trend of low-D anomalies in the western region while high-D anomalies in the eastern. As it is shown in the figure 5f, in the inner TP, low-D anomalies are blocked, whist high-D anomalies are outside the TP. The low-D anomalies in TP illustrate the existence of hot weak material beneath the TP, which is beneficial to the external material inward-thrusting. It is interesting to note that on the eastern TP, beneath all the recent earthquakes epicenters (WCH- earthquake epicenter Wenchuan, LSH- earthquake epicenter Lushan, LD-earthquake epicenter Ludian, YJ- earthquake epicenter Yingjiang), the density anomalies at this depth are high.

5. Discussion

Studies of deep seismic soundings showed that the northern edge of the Indian crust is about 50 – 100 km south of BNS (east of 90E)[7]. Receiver function results signified that Indian crust can be traced to 31°N[1]. However, P wave tomography derived by Zhao et al. showed that the Indian Plate is currently sub-horizontal and under-thrusting to the JRS at depths from ~100 to ~250 km[33]. High velocity zone (HVZ) estimated by P wave tomography inferred that Indian plate underlies only the southwestern plateau[34]. Similar to HVZ, the high-D anomalies also trace the subduction of the Indian Plate's and they can give how far the Indian lithospheric plate subducts beneath the Tibetan Plateau. Our results show that high-D anomalies are predominant in the southwestern TP (Himalaya block, Lhasa block, Qiangtang block) at 0-300 km depth with terminating around Jinsha River Suture (JRS) from the south. Based on the range of high-D anomalies inside the TP, we can infer that the under-thrusting Indian plate has been reached over the Bangong Nujiang Suture (BNS) and almost reach to the JRS at the depth greater than 300 km.

P wave tomography constructed by Lei and Zhao found that road high-V anomalies are visible from the Burma arc northward in the mantle transition zone (MTZ) beneath Eastern Tibet, as is the case in several other studies[35-37] and it has been inferred that they may represent the eastward subduction of the Indian slab along the Burmese arc. Our high-D anomalies are at the depth of 400-500 km (the depth of mantel transition zone, MTZ) give further evidence to the eastward subduction.

Teleseismic P-wave tomography shows that the velocities are lower in both the lower crust and uppermost mantle under southwestern Yunnan from regional waveform inversion[38]. High Poisson's ratio and thin crust are beneath the Yunnan region[39]. In our results, low-D anomalies image both in the crust and lithospheric mantel (at the 0-300 km depth). As analogous to the velocity anomalies, Low-D anomalies in the crust is the result of the extruded of Indian Plate and the obstruction by the surrounding hard blocks[40]. This gives a higher temperature and lower Poisson's ratio in the lower crust. Low-D anomalies in the lithospheric mantle can be contributed by the deep slab dehydration Low-D anomalies in the MTZ are the subducted heavy plate. This provides forces and environments to the occurrence of the frequent earthquakes[41] (Wenchuan earthquake with magnitude of 8.0 in 2008; Lushan earthquake with magnitude of 7.0 in 2013; Ludian earthquake with magnitude of 6.5 in 2014; Yingjiang earthquake with magnitude of 6.5) and the generation of Tengchong volcano at this area.

In the south, the Indian Plate underthrusts Tibet. In central and northern Tibet, a separate, thin Tibet Plate exists, underthrust by the Asian Plate from the north[42, 43]. The hot thermal anomalies exist[11]. At the average depth of 600 km, low-D anomalies present inside the whole TP, in combination with high-D anomalies outside the TP, thus giving rise to the incidental inward-thrusting from the cold hard external TP to the hot weak internal TP.

6. Conclusions

In this paper, we presented the inversion of the geoid in both simulation and real cases. The geoid anomaly could provide long-wavelength detailed density features underground. We obtained a three-dimensional crustal and upper mantel structures beneath the eastern margin of Tibet Plateau. We summarize our major findings as follows.

(1). A certain degree of consistency of the density anomalies features at the depth from 0 km to 300 km, except those in the middle Songpan Ganzi, indicating the coupling of crust and upper mantel.

(2). At 0-300 km depth, high density (high-D) anomalies are apparent in the southwestern TP with terminating around Jinsha River Suture (JRS) from the south. This illustrates that the under-thrusting Indian plate has been reached over the Bangong Nujiang Suture (BNS) and almost reach to the JRS at the depth greater than 300 km.

(3). On the eastern TP, density features that high density anomalies are at the depth of 400-500 km (the depth of mantel transition zone, MTZ) while lower density (low-D) anomalies are at the depth of 100-300 km (the depth of upper mantel). Low velocities in the crust and uppermost mantle and high velocities in the MTZ beneath this region further verify the current eastward subduction of Indian plate along the Burma arc. The ongoing subduction provides forces and environments to the occurrences of frequent earthquakes and the generation of Tengchong volcano in this area.

(4). At 600 km depth, low-D anomalies present inside the whole TP along with high-D anomalies outside the TP, thus accounting for the incidental inward-thrusting from the cold hard external TP to the hot weak internal TP.

Acknowledgments: We great acknowledge the Major State Basic Research Development Program of China 973 Program 2013CB733301 and the National Natural Science Fund 41274025 for supporting the work. We appreciate the sharing of S-wave velocity. The U.S. National Geospatial Intelligence Agency (NGA) is thanked for the use of the EGM2008 data. We also acknowledge the use of Generic Mapping Tool (GMT).

Author Contributions: Jian Fang provided the initial idea for this study; Honglei Li conceived and designed all the inversion synthetic experiments and the application in the eastern Qinghai-Tibetan Plateau; Honglei Li and Jian Fang analyzed the experiment results; Honglei Li wrote the paper.

Conflicts of Interest: The authors declare no conflict of interest.

References

1. Nábělek, J.; Hetényi, G.; Vergne, J.; Sapkota, S.; Kafle, B.; Jiang, M.; Su, H.; Chen, J.; Huang, B.-S. Underplating in the Himalaya-Tibet collision zone revealed by the Hi-CLIMB experiment. Science 2009, 325, (5946), 1371-1374.
2. Molnar, P. A review of geophysical constraints on the deep structure of the Tibetan Plateau, the Himalaya and the Karakoram, and their tectonic implications. Philosophical Transactions of the Royal Society of London A: Mathematical, Physical and Engineering Sciences 1988, 326, (1589), 33-88.
3. Ji-wen, T. My understand and ponder for few important kernel problems in and great achievements for first time and developmental direction of Geophysical research in Tibetan Plateau of China [J]. Progress in Geophysics 2008, 2, 002.
4. Bourjot, L.; Romanowicz, B. Crust and upper mantle tomography in Tibet using surface waves. Geophysical Research Letters 1992, 19, (9), 881-884.
5. Kind, R.; Yuan, X.; Saul, J.; Nelson, D.; Sobolev, S.; Mechie, J.; Zhao, W.; Kosarev, G.; Ni, J.; Achauer, U. Seismic images of crust and upper mantle beneath Tibet: evidence for Eurasian plate subduction. Science 2002, 298, (5596), 1219-1221.
6. Li, S.; Mooney, W. D. Crustal structure of China from deep seismic sounding profiles. Tectonophysics 1998, 288, (1), 105-113.
7. Zhang, Z.; Deng, Y.; Teng, J.; Wang, C.; Gao, R.; Chen, Y.; Fan, W. An overview of the crustal structure of the Tibetan plateau after 35 years of deep seismic soundings. Journal of Asian Earth Sciences 2011, 40, (4), 977-989.
8. Bai, D.; Unsworth, M. J.; Meju, M. A.; Ma, X.; Teng, J.; Kong, X.; Sun, Y.; Sun, J.; Wang, L.; Jiang, C. Crustal deformation of the eastern Tibetan plateau revealed by magnetotelluric imaging. Nature geoscience 2010, 3, (5), 358-362.
9. Sun, J.; Jin, G.; Bai, D.; Wang, L. Sounding of electrical structure of the crust and upper mantle along the eastern border of Qinghai-Tibet Plateau and its tectonic significance. Science in China Series D: Earth Sciences 2003, 46, (2), 243-253.
10. Mahéo, G.; Guillot, S.; Blichert-Toft, J.; Rolland, Y.; Pêcher, A. A slab breakoff model for the Neogene thermal evolution of South Karakorum and South Tibet. Earth and Planetary Science Letters 2002, 195, (1), 45-58.
11. McKenzie, D.; Jackson, J.; Priestley, K. Thermal structure of oceanic and continental lithosphere. Earth and Planetary Science Letters 2005, 233, (3), 337-349.
12. Chaves, C. A. M.; Ussami, N. Modeling 3-D density distribution in the mantle from inversion of geoid anomalies: Application to the Yellowstone Province. Journal of Geophysical Research: Solid Earth 2013, 118, (12), 6328-6351.
13. LaCoste, L. J. Measurement of gravity at sea and in the air. Reviews of Geophysics 1967, 5, (4), 477-526.
14. Zhao, L.; Wu, M.; Forsberg, R.; Olesen, A. V.; Zhang, K.; Cao, J. Airborne Gravity Data Denoising Based on Empirical Mode Decomposition: A Case Study for SGA-WZ Greenland Test Data. ISPRS International Journal of Geo-Information 2015, 4, (4), 2205-2218.
15. Pavlis, N. K.; Holmes, S. A.; Kenyon, S. C.; Factor, J. K. An earth gravitational model to degree 2160: EGM2008. EGU General Assembly 2008, 13-18.
16. Zhang, C. Y.; Guo., C. X.; Chen, J. Y. ; Zhang, L. M.; Wang, B. EGM 2008 and Its Application Analysis in Chinese Ma inland. Acta Geodaetica et Cartographica Sinica 2009, 38, (4), 0-310.
17. Heiskanen, W. A.; Moritz, H. Physical geodesy. Bulletin Géodésique (1946-1975) 1967, 86, (1), 491-492.
18. Heck, B.; Seitz, K. A comparison of the tesseroid, prism and point-mass approaches for mass reductions in gravity field modelling. Journal of Geodesy 2007, 81, (2), 121-136.
19. Tikhonov, A. N.; Arsenin, V. Y. Solutions of ill-posed problems. 1977.
20. Klemperer, S. L. Crustal flow in Tibet: geophysical evidence for the physical state of Tibetan lithosphere, and inferred patterns of active flow. Geological Society, London, Special Publications 2006, 268, (1), 39-70.
21. Zhang, P.; Deng, Q.; Zhang, G.; Ma, J.; Gan, W.; Min, W.; Mao, F.; Wang, Q. Active tectonic blocks and strong earthquakes in the continent of China. Science in China Series D: Earth Sciences 2003, 46, (2), 13-24.
22. Bowin, C. Depth of principal mass anomalies contributing to the earth's geoidal undulations and gravity anomalies©. Marine Geodesy 1983, 7, (1-4), 61-100.

Peer-reviewed version available at *ISPRS Int. J. Geo-Inf.* **2017**, *6*, 4; doi:10.3390/ijgi6010004

23. Amante, C.; Eakins, B. ETOPO1 1 Arc-Minute Global Relief Model: Procedures, Data Sources and Analysis. NOAA Technical Memorandum NESDIS NGDC-24. National Geophysical Data Center. Biblioteca Digital ILCE 2009, 1.
24. Fang, J.; Xu, H. Three dimensional distribution of liothsperic density beneath the china and its anjacent region. Chinese Journal Geophysics 2002, 45, (1), 42-48.
25. Laske, G.; Masters, G.; Ma, Z.; Pasyanos, M. CRUST1. 0: An updated global model of Earth's crust. Geophys Res Abs 2012, 14.
26. Pasyanos, M. E.; Masters, T. G.; Laske, G.; Ma, Z. LITHO1. 0: An updated crust and lithospheric model of the Earth. Journal of Geophysical Research: Solid Earth 2014, 119, (3), 2153-2173.
27. Woodhouse, J. H.; Dziewonski, A. M. Mapping the upper mantle: Three-dimensional modeling of Earth structure by inversion of seismic waveforms. Journal of Geophysical Research: Solid Earth 1984, 89, (B7), 5953-5986.
28. Simmons, N. A.; Forte, A. M.; Boschi, L.; Grand, S. P. GyPSuM: A joint tomographic model of mantle density and seismic wave speeds. Journal of Geophysical Research: Solid Earth 2010, 115, (B12).
29. Yang, Y.; Ritzwoller, M. H.; Zheng, Y.; Shen, W.; Levshin, A. L.; Xie, Z. A synoptic view of the distribution and connectivity of the mid-crustal low velocity zone beneath Tibet. Journal of Geophysical Research: Solid Earth 2012, 117, (B4).
30. Wang, X.; Fang, J.; Hsu, H. Three-dimensional density structure of the lithosphere beneath the North China Craton and the mechanisms of its destruction. Tectonophysics 2014, 610, 150-158.
31. Liang, C.; Song, X. A low velocity belt beneath northern and eastern Tibetan Plateau from Pn tomography. Geophysical Research Letters 2006, 33, (22).
32. Lei, F.; Qu, Y.; Song, G. Species diversification and phylogeographical patterns of birds in response to the uplift of the Qinghai-Tibet Plateau and Quaternary glaciations. Current Zoology 2014, 60, (2), 149-161.
33. Zhao, J.; Zhao, D.; Zhang, H.; Liu, H.; Huang, Y.; Cheng, H.; Wang, W. P-wave tomography and dynamics of the crust and upper mantle beneath western Tibet. Gondwana Research 2014, 25, (4), 1690-1699.
34. Zhao, J.; Yuan, X.; Liu, H.; Kumar, P.; Pei, S.; Kind, R.; Zhang, Z.; Teng, J.; Ding, L.; Gao, X. The boundary between the Indian and Asian tectonic plates below Tibet. Proceedings of the National Academy of Sciences 2010, 107, (25), 11229-11233.
35. Lei, J.; Zhao, D. Teleseismic P-wave tomography and mantle dynamics beneath Eastern Tibet. Geochemistry, Geophysics, Geosystems 2016.
36. Sun, X.; Bao, X.; Xu, M.; Eaton, D. W.; Song, X.; Wang, L.; Ding, Z.; Mi, N.; Yu, D.; Li, H. Crustal structure beneath SE Tibet from joint analysis of receiver functions and Rayleigh wave dispersion. Geophysical Research Letters 2014, 41, (5), 1479-1484.
37. Li, C.; Van der Hilst, R. D.; Meltzer, A. S.; Engdahl, E. R. Subduction of the Indian lithosphere beneath the Tibetan Plateau and Burma. Earth and Planetary Science Letters 2008, 274, (1), 157-168.
38. Li, Y.; Wu, Q.; Zhang, R.; Tian, X.; Zeng, R. The crust and upper mantle structure beneath Yunnan from joint inversion of receiver functions and Rayleigh wave dispersion data. Physics of the Earth and Planetary Interiors 2008, 170, (1), 134-146.
39. Zha, X. H.; Lei, J. S. Crustal thickness and Poisson's ratio beneath the Yunnan region. Science China: Earth Sciences 2013, 43, 446-456.
40. Lei, J.; Li, Y.; Xie, F.; Teng, J.; Zhang, G.; Sun, C.; Zha, X. Pn anisotropic tomography and dynamics under eastern Tibetan plateau. Journal of Geophysical Research: Solid Earth 2014, 119, (3), 2174-2198.
41. Lei, J.; Zhao, D.; Su, Y. Insight into the origin of the Tengchong intraplate volcano and seismotectonics in southwest China from local and teleseismic data. Journal of Geophysical Research: Solid Earth 2009, 114, (B5).
42. Zhao, D.; Pirajno, F.; Dobretsov, N. L.; Liu, L. Mantle structure and dynamics under East Russia and adjacent regions. Russian Geology and Geophysics 2010, 51, (9), 925-938.
43. Zhao, L.; Zheng, T.; Lu, G. Distinct upper mantle deformation of cratons in response to subduction: constraints from SKS wave splitting measurements in eastern China. Gondwana Research 2013, 23, (1), 39-53.